Magnetic Resonance Materials in Physics, Biology and Medicine (2022) 35:557–571
https://doi.org/10.1007/s10334-022-01012-8

REVIEW

MR fingerprinting of the prostate

Wei-Ching Lo[1,2] · Ananya Panda[3] · Yun Jiang[4] · James Ahad[5] · Vikas Gulani[4] · Nicole Seiberlich[4,5]

Received: 16 July 2021 / Revised: 21 March 2022 / Accepted: 24 March 2022 / Published online: 13 April 2022

Abstract

Multiparametric magnetic resonance imaging (mpMRI) has been adopted as the key tool for detection, localization, characterization, and risk stratification of patients suspected to have prostate cancer. Despite advantages over systematic biopsy, the interpretation of prostate mpMRI has limitations including a steep learning curve, leading to considerable interobserver variation. There is growing interest in clinical translation of quantitative imaging techniques for more objective lesion assessment. However, traditional mapping techniques are slow, precluding their use in the clinic. Magnetic resonance fingerprinting (MRF) is an efficient approach for quantitative maps of multiple tissue properties simultaneously. The T_1 and T_2 values obtained with MRF have been validated with phantom studies as well as in normal volunteers and patients. Studies have shown that MRF-derived T_1 and T_2 along with ADC values are all significant independent predictors in the differentiation between normal prostate tissue and prostate cancer, and hold promise in differentiating low and intermediate/high-grade cancers. This review seeks to introduce the basics of the prostate MRF technique, discuss the potential applications of prostate MRF for the characterization of prostate cancer, and describes ongoing areas of research.

Keywords Magnetic resonance imaging · Quantitative imaging · Prostate · Magnetic resonance fingerprinting

Introduction

The role of multiparametric magnetic resonance imaging (mpMRI) for the detection, localization, and locoregional staging of prostate cancer has grown over the past two decades [1–3]. Cancer suspicious lesions can be seen on MR using T_2-weighted and diffusion-weighted images (DWI) and apparent diffusion coefficient (ADC) maps, and often as early enhancing foci on dynamic contrast-enhanced (DCE) images. For this reason, MRI has become the gold-standard imaging modality for the assessment of the prostate, and mpMRI the protocol of choice. mpMRI imaging has also been deployed to assist in biopsy targeting, leading to a higher detection of clinically significant cancer and reduced detection of indolent lesions as compared to standard transrectal ultrasound (TRUS) biopsy [4].

The mpMRI protocol of the prostate typically includes T_2-weighted images for anatomical assessment along with DWI and DCE MRI. Interpretation of mpMRI is guided by the recommendations provided by the Prostate Imaging Reporting and Data System version 2.1 (PI-RADS v2.1) [5]. The evaluation of mpMRI is a qualitative assessment which may lead to differences in interpretation between different readers [6]. There has been increased exploration of the use of quantitative tissue property mapping for disease diagnosis and staging, as these maps may provide more objective information than conventional weighted imaging. In particular, ADC measurements derived from DWI have been suggested as a potential adjunct to qualitative analysis in PI-RADS [7–10]. Quantitative mapping of T_1 and T_2 is not routinely performed or included in PI-RADS due to the time needed to make these maps, and their unknown marginal utility in assessing for prostate cancer.

Recently, several approaches for quantitative T_1 and T_2 mapping have emerged and been applied in the prostate, with

✉ Nicole Seiberlich
nse@med.umich.edu

[1] Department of Biomedical Engineering, Case Western Reserve University, Cleveland, OH, USA

[2] Siemens Medical Solutions USA, Boston, Massachusetts, USA

[3] Department of Radiology, Mayo Clinic, 200 1st Street SW, Rochester, MN 55905, USA

[4] Department of Radiology, University of Michigan, University of Michigan Health System, 1500 E. Medical Center Drive, Ann Arbor, MI 48109-5030, USA

[5] Case Western Reserve University, Cleveland, OH, USA

the goal of improving the reproducibility of cancer assessment through the objective use of tissue property values to diagnose and stratify disease. Magnetic Resonance Fingerprinting (MRF), a technique which enables the simultaneous generation of quantitative maps of multiple tissue properties [11, 12], has also been explored in the prostate [13–17]. While the primary benefit of deploying MRF in the prostate is the ability to rapidly characterize prostate tissues, MRF may offer additional advantages over conventional mapping approaches. For example, early work has shown that MRF data can be used to extract information about individual tissue components [18, 19], potentially enabling improved discrimination of disease. Moreover, it has been suggested that MRF-derived tissue property maps can be combined with machine learning for automatic lesion detection [20]. The efficiency, reproducibility, and potential sensitivity to changes in prostate tissue, along with the possibility of efficient post-processing and analysis, makes MRF an exciting new tool in clinical prostate assessment.

This review seeks to introduce the basics of MRF for tissue property mapping in the prostate, including pulse sequence design, dictionary generation, and tissue property map reconstruction algorithms. The potential applications in prostate imaging are also discussed, and current limitations and ongoing areas of research are described.

The mpMRI protocol

Each of the images acquired in an mpMRI protocol serves a different purpose. T_2-weighted imaging reflects the water content and cellularity of the tissue, and is used as a high-resolution anatomical image of the zonal structure due to the excellent soft tissue contrast [21, 22]. T_2-weighted imaging plays a primary role in evaluation of transition zone (TZ) lesions, and a secondary role to diffusion-weighted imaging for evaluation of peripheral zone (PZ) lesions. In the normal prostate, the PZ appears hyperintense on T_2-weighted imaging (though benign changes such as prostatitis can be hypointense), while the TZ has a heterogeneous appearance with areas of hypo-intensity and hyper-intensity [23, 24]. T2w imaging also plays an important role in characterizing TZ lesions, as BPH nodules common in the TZ may exhibit restricted diffusion which can decrease sensitivity in identifying prostate cancer using diffusion-weighted images. However, intensity alone cannot be used as an objective measurement of grade, because the degree of hypo-intensity varies from manufacturer to manufacturer, with sequence and user-controlled settings, and across scanners.

DWI provides qualitative and quantitative information about cellularity and the degree of motion of water molecules within tissue. Prostate cancer appears hyperintense on DWI due to the increased cellularity and reduced diffusion coefficients compared with healthy tissue [25]. A decrease in the ADC value, calculated from multiple diffusion-weighted images with different b values, is associated with increasing Gleason score [26, 27]. The use of both DWI and T_2-weighted imaging results in higher sensitivity and specificity than T_2-weighted imaging alone for detecting prostate cancer in both PZ and TZ [28, 29].

In addition to the essential T_2-weighted images and ADC maps, DCE MRI images can be used to assess perfusion. DCE MRI images are generated by acquiring a series of T_1-weighted images before and dynamically after the injection of a gadolinium-based contrast agent. These images show early focal enhancement in prostate cancer [30]. While DCE images can be processed to yield quantitative maps of perfusion-related parameters, these measurements suffer from poor repeatability and reproducibility, preventing this information from being used in standard clinical practice [31]. Although a semi-quantitative analysis of the shape of the DCE signal enhancement curve was originally included in PI-RADS v1, curve shape was not specific enough to warrant inclusion in PI-RADS v2.1. As it currently stands in PI-RADS v2.1, DCE imaging is used only to upgrade risk of peripheral zone lesions from Category 3 to 4 via visual assessment of DCE images, with cancers tending enhance earlier or simultaneously with surrounding normal tissue [32]. While T_1-weighted imaging itself plays no diagnostic role for prostate cancer detection, as both cancer and normal tissue have low and homogeneous signal intensity [22], T1-weighted images are generally used to assess for presence of hemorrhage (which can confound T2w and diffusion imaging) and for DCE analysis [33].

Once relevant images have been acquired, the presence and stage of prostate cancer can be assessed using the criteria laid out in the PI-RADS v2.1 five point scoring system. However, PI-RADS has a number of limitations [34, 35]. Besides ADC maps, the images used in PI-RADS are qualitative, meaning that they do not reflect measurements of tissue properties (such as T_2) but are merely images which are weighted by these tissue properties. As such, prostate tissues cannot be objectively evaluated to determine if a suspicious lesion has tissue properties that mark it as different from healthy tissue. As these images are approached somewhat subjectively, PI-RADS suffers from limited inter-reader agreement, even between experienced readers [34]. There is also a learning curve associated with PI-RADS interpretation, which may contribute to this lack of agreement [36, 37]. A more objective approach to the assessment of the health of the prostate gland may reduce these discrepancies and enable a more definitive evaluation.

Conventional approaches for quantitative tissue property mapping in the prostate

Although the analysis of quantitative maps beyond ADC is currently not part of PI-RADS v2.1, there are reasons to believe that changes to prostate tissue may be measured through quantitative tissue property mapping. Using conventional relaxometry approaches, T_2 values have been observed across multiple studies to be higher in PZ than TZ, and higher in normal tissue as compared to cancer [38, 39]. Multiple groups have shown that T_2 mapping can be used to distinguish normal prostate tissue, prostatitis, and benign prostatic hyperplasia (BPH) from prostate cancer [40–45]. Decreased T_2 and ADC values have been reported in prostate cancer tissue as compared to healthy tissue, and these values correlated with the aggressiveness of the prostate cancer [27, 46–51]. It has been suggested that T_2 mapping can add higher positive predictive value to prostate cancer evaluation, as compared to T2w imaging alone.

Unlike T_2 mapping, T_1 mapping has not been explored in depth, presumably due to the fact that T_1-weighted images are not widely used for prostate cancer evaluation because they exhibit little contrast between cancer and normal prostate tissue. However, in a small recent study of 23 patients, it was found that T_1 is lower in prostate cancer as compared to benign prostatic tissue [52]. Using a dual echo turbo spin echo saturation recovery (four delay times) acquisition for T_1 and T_2 mapping, T_1 and T_2 times in cancer were found to be lower than stromal hyperplasia and noncancerous PZ, though TZ and PZ cancers were not separated and overall diagnostic performance was lower than ADC [53].

Several groups have attempted to understand the histological underpinnings of measured relaxation property differences in prostate tissues and cancer [54].For example, Sabouri et al. have assessed the feasibility of luminal water fraction determination on the basis of T_2 mapping for detecting and grading prostate cancer [55]. The quantitation of prostatic lumen, stroma and epithelium has been explored using compartment modeling of T_2 and ADC mapping data, where it was reported that fractional epithelium volume is increased, and lumen and stroma are decreased in the presence of cancer [56].

However, conventional T_1 and T_2 mapping sequences can be slow and inefficient. The Modified Look-Locker inversion recovery sequence (MOLLI) used for T_1 mapping required a data acquisition time of 4.5 min for maps with a resolution of $1.3 \times 1.3 \times 3$ mm^3 [52]. For T_2 mapping using a multi-echo turbo spin echo approach with an interpolated resolution of $0.55 \times 0.76 \times 2.2$ mm^3, the acquisition time was 2 min and 24 s [50]. Because T_1 and T_2 mapping is time-consuming and these maps are not typically acquired, these measurements made via conventional approaches have not been thoroughly assessed for their use in tissue characterization and cancer detection.

Magnetic resonance fingerprinting

Magnetic resonance fingerprinting (MRF) [11] is an approach for quantitative tissue property mapping that can be used to efficiently generate maps of multiple tissue properties simultaneously. MRF has been used in a number of organs for the acquisition of T_1 and T_2 maps, including the brain [11, 57, 58], abdominal organs [59], heart [60], breast [61, 62], and prostate [13–15]. The general MRF framework consists of four key components: MRF data acquisition, image timeseries reconstruction, dictionary simulation, and map generation. An overview of the MRF workflow is shown in Fig. 1 and described in the following sections.

MRF data acquisition

MRI signals can be sensitized to tissue properties, such as T_1 and T_2, by selecting appropriate pulse sequence parameters, i.e., the repetition time (TR), echo time (TE), flip angle (FA), etc. MRF pulse sequences are specially designed so that different tissues (assumed to have different T_1 and/or T_2 values) to give rise to signals with different profiles over time, and that these signals can be distinguished from one another. Typically in MRF, the TR and FA are varied in a controlled fashion to ensure that these signals are unique, and data acquisition is often initialized with an inversion pulse to boost the sensitivity of the signal to T_1. T_2-preparation pulses and additional inversion pulses can also be used to increase this sensitivity to T_2 and T_1, respectively. Delay times may also be inserted to ensure that signals arising from tissues with different tissue properties can be distinguished from one another. While the first MRF sequence used in the brain was based on a balanced steady-state free precession (bSSFP) readout [11], any sequence structure is can be used along with MRF. The selection of a pulse sequence structure depends on the tissue properties to measured; the fast imaging with steady-state precession (FISP) readout is increasingly deployed in MRF due to its relative insensitivity to off-resonance effects [12].

There are many different ways to select the pulse sequence parameters for an MRF acquisition. While the original MRF work used several empirically chosen combinations of TR and flip angle [11], other groups have used brute force approaches [63], testing many different possible scanner parameters and selecting the one that gives the best accuracy for the tissue property maps. More refined approaches include using quality factors based on noise figures [64], Cramer-Rao Lower Bounds [65], computer models combined with physics-inspired optimization heuristics [66],

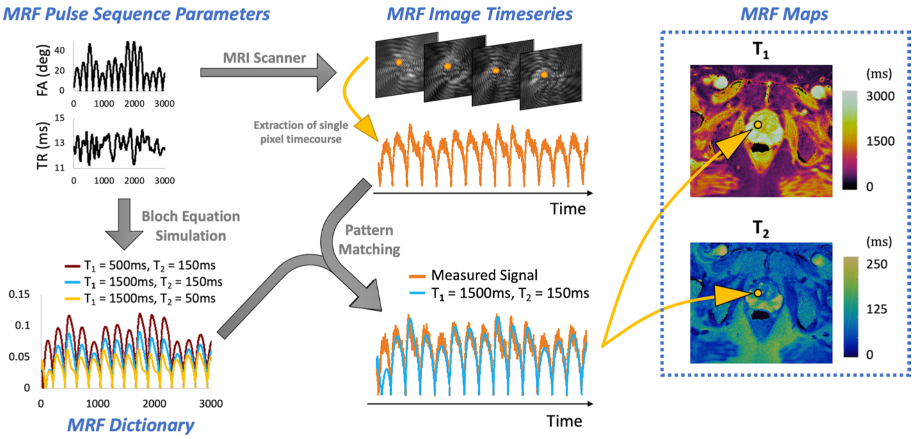

Fig. 1 Overview of the MRF workflow. (Left top) Data are acquired using an MRF pulse sequence with variable acquisition settings (FA and TR). (Left bottom) The MRF pulse sequence parameters and a large set of tissue property values (i.e., T_1 and T_2) are entered as inputs to a Bloch equation simulation to generate the MRF dictionary. (Middle top) The MRF pulse sequence is used to collect highly accelerated images at the MRI scanner; the signal timecourse of one voxel over time (orange curve) is dictated by the properties of the tissue in that voxel along with the pulse sequence settings. (Middle bottom) The measured signal from one voxel is compared to the dictionary in the pattern matching step and the best match found. (Right) The tissue properties used to make the best matching dictionary entry are assigned as the T_1 and T_2 values for that voxel, and the process repeated for all voxels

and deep learning [67]. An excellent overview of different MRF pulse sequence parameter optimization approaches can be found in [68].

MRF data are usually acquired along non-Cartesian sampling trajectories where each acquisition window (i.e., data acquired in a single TR) provides unique information about the underlying tissue properties. To effectively extract this information, specialized techniques must be deployed, which will be outlined below.

MRF image timeseries generation

Once the MRF data have been acquired, these data are converted into images, which are used in the later pattern matching step. Originally, the data acquired in each TR of the acquisition were transformed to the image domain via the non-uniform fast Fourier transform (NUFFT [69]), resulting in a timeseries of images. Given the high data undersampling factor, the MRF images are significantly corrupted by aliasing artifacts. However, when using non-Cartesian trajectories like spirals or radial, these aliasing artifacts appear noise-like in the images. Recently, approaches for reducing the artifacts in these individual images have been introduced into the pipeline, including view-sharing [70], parallel imaging [71], iterative de-noising [72], and low-rank/compressed sensing reconstructions [73–77]. However, these image reconstruction steps are not required in MRF, where the accelerated images can be used in the subsequent tissue property extraction steps despite the presence of significant aliasing artifacts.

After conversion to the image domain, images acquired with multiple receiver coils are combined using adaptive coil combination [78]. Recent works have suggested that further processing steps can be accelerated by compressing the MRF raw data or images along the coil dimension using PCA [79] or along the time dimension using singular value decomposition compression [76, 80]. Once the timeseries of images has been prepared, it can be used for further processing to extract tissue property information (see below).

MRF dictionary simulation

The MRF reconstruction relies on the knowledge of the relationship between signal evolutions acquired at the MRI scanner and tissue properties (T_1, T_2, etc.). In most conventional mapping techniques, the relationship between a tissue property and signal evolution is described by an exponential signal model, and quantitative tissue property values can be extracted by curve fitting the observed signal to the model. However, in MRF, the relationship between tissue properties and the signal evolutions is designed to be far more complex by varying pulse sequence parameters throughout the acquisition. To efficiently match the measured signal time courses in MRF to the appropriate combination of tissue property values, dictionary matching approaches are typically used in place of explicit curve fitting.

In MRF, the signal time course that arises from a voxel is a consequence of both the sequence parameters used in the acquisition (such as FAs and TRs) as well as the properties (i.e., T_1 and T_2) of the tissue in that voxel. The signal evolutions that would result from the applied MRF pulse sequence for different combinations of T_1 and T_2 are calculated. Once the timeseries for a set of tissue properties has been calculated, it is normalized for later use in pattern matching, and deposited as an entry in the dictionary. These MRF signal time courses can be calculated using a variety of techniques, where the most common is through the use of Bloch Equation simulations. Other approaches include modeling signals using Extended Phase Graphs (EPG) [81, 82], or training a neural network to recapitulate the Bloch Equations in a significantly shorter time than explicit Bloch equation calculations [83].

The expected physiological range of tissue properties for the target clinical applications is used to define the upper and lower boundary of the T_1 and T_2 values for which dictionary entries are calculated. For example, an MRF dictionary may contain signal evolutions for combinations of T_1 values from 10 to 3000 ms with an increment of 10 ms, and T_2 values from 2 to 500 ms with an increment of 2 ms. Note that both the accuracy and precision of the mapped T_1 and T_2 values are determined in part by the MRF dictionary resolution. If the dictionary resolution is fine (with small spacing between T_1 and T_2 entries), the size of the MRF dictionary can be quite large and challenging to work with, but the signal evolutions may be more accurately represented in the dictionary. On the other hand, if the dictionary resolution is coarse, the size of the MRF dictionary will be small, but the entries may not be truly representative of the signal evolutions found in the acquired data. Also note that the dictionary size grows exponentially with the number of tissue properties to be mapped in the MRF scan; a large dictionary increases the computational load and memory requirements for the reconstruction. This dictionary size consideration may limit the number of individual tissue properties that can realistically be assessed in an MRF scan.

MRF map generation

The final step in the MRF pipeline is to match the MRF image timeseries to the dictionary to select the dictionary entry that best represents the acquired signal for each voxel. The T_1 and T_2 values that went into constructing that entry can then be assigned to that voxel as the measured values. There are several approaches to this step, but the most commonly used (and simplest) is known as cross-correlation pattern matching. Here, the signal from a single pixel through time is extracted from the image timeseries, and normalized. The cross-correlation (inner product) between this measured signal and all of the dictionary entries is calculated, and the dictionary entry with the highest cross-correlation value is selected as the best "match". The T_1 and T_2 values which were used to construct that dictionary entry are then assigned as the tissue properties of that voxel.

This simple matching process may be slow, especially if the dictionary is large. To combat these effects, more advanced matching approaches may be used, such as fast group matching [84]. Machine learning approaches have also evolved, in which the tissue properties can be extracted from the data without the need for an explicit dictionary [85–90]. These approaches may be especially useful in situations where the dictionary can become very large, for instance when mapping more than two tissue properties [91].

Prostate MRF

Prostate MRF acquisition and tissue property map generation

The MRF sequence which has primarily been deployed for the assessment of prostate patients thus far was developed for use at 3 T and is described in [13]. However, other different implementations of MRF could be used to measure T_1 and T_2, such as that described in [17]. The sequence reported in [13] is based on FISP MRF [12] due its relative insensitivity to off-resonance effects in the presence of field inhomogeneities from sources such as bowel gas. A schematic of this pulse sequence is shown in Fig. 2. The magnetization is first prepared by applying an inversion pulse, followed by the acquisition of 3000 blocks of data, with TRs varying between 11.2 and 14.2 ms and flip angles varying between 0° and 50°, as shown in Fig. 1. This TR series was selected using a Perlin noise pattern, and the flip angles were varied in a sinusoidal pattern, where the maximum flip angle was randomly selected as described in detail

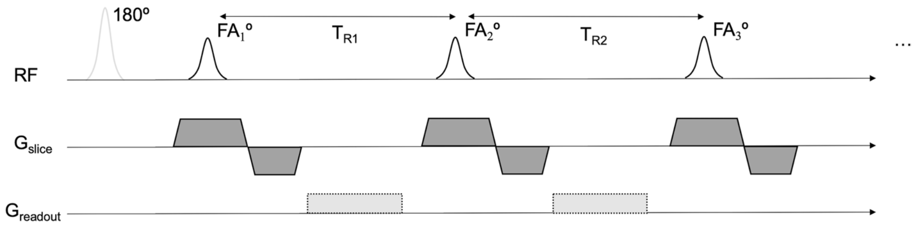

Fig. 2 A schematic of the pulse sequence used for prostate MRF at 3 T. The readout used in many implementations is a uniform density spiral. The repetitions times (TR) and flip angles (α) change after each data acquisition block, and are shown on the left hand side of Fig. 1

in [12]. Additionally, short relaxation periods with a length of 10 TRs were inserted every 200 TRs. Data collection is performed using a uniform density spiral readout. The data matrix is 400 × 400, with a field-of-view of 400 × 400 mm^2, leading to an in-plane resolution of 1 × 1 mm^2, with slice thicknesses ranging from 3 to 6 mm. The total acquisition time for this prostate MRF implementation is 39 s for one slice, and a delay time of at least 5 s is inserted between measurements to ensure sufficient magnetization recovery before beginning the next experiment. After the acquisition, the raw data are compressed along the coil dimension to eight virtual coils, and an SVD is performed along the time dimension to compress the timeseries from 3000 points to 43. The compressed data are converted to the image domain using the NUFFT.

In prostate MRF, the MRF dictionary can be pre-calculated, as the sequence parameters are not altered from subject to subject. In the prostate and pelvic area, the T_1 is expected to range between 1000 and 2500 ms, and the T_2 between 20 and 300 ms for 3 T systems [15]. Dictionary resolutions, here listed in ms with a format of [min:step:max], for T_1 values are [10:5:90, 100:10:1000, 1020:20:1500, 1550:50:2050, 2150:100:2950] and T_2 values are [2:2:10, 15:5:150, 160:10:200, 250:50:500], where values of T_1 which are less than T_2 are excluded. This dictionary has a total of 5,970 entries. Like the collected timeseries data, the dictionary is compressed along the timeseries direction, yielding 43 timepoints. Then the cross-correlation between the collected timeseries for a single voxel and each dictionary entry is calculated to find the T_1 and T_2 value for the voxel. This reconstruction can be performed off-line (for instance, in Matlab), but has also been implemented on the Gadgetron platform for rapid, on-line reconstruction and simplified clinical deployment [16].

Application of prostate MRF

Prostate MRF has been explored for the characterization of prostate pathologies in both the peripheral and transition zones [13–15]. An example of a T_1 map and a T_2 map generated using prostate MRF at 3 T, along with an ADC map and T_2-weighted image, are shown in Fig. 3. This patient has prostate cancer (Gleason grade 9) with PZ involvement, marked with a white arrow. Note the hypo-intensity of the cancer in the T_2-weighted image, and the low value of the ADC in this region. The MRF-derived T_1 and T_2 maps are shown at the bottom. The mean T_1 and T_2 values in this prostate cancer were significantly lower than normal PZ (T_1 was 1533 ± 175 ms vs. 2920 ± 80 ms, and T_2 was 37 ± 7 ms vs. 261 ± 57 ms), where the ROIs analyzed are marked with black borders on the MRF maps.

The initial prostate MRF work focused on quantitative lesion characterization in the PZ [13]. MRF and ADC data, in addition to standard T_2-weighted images, were collected

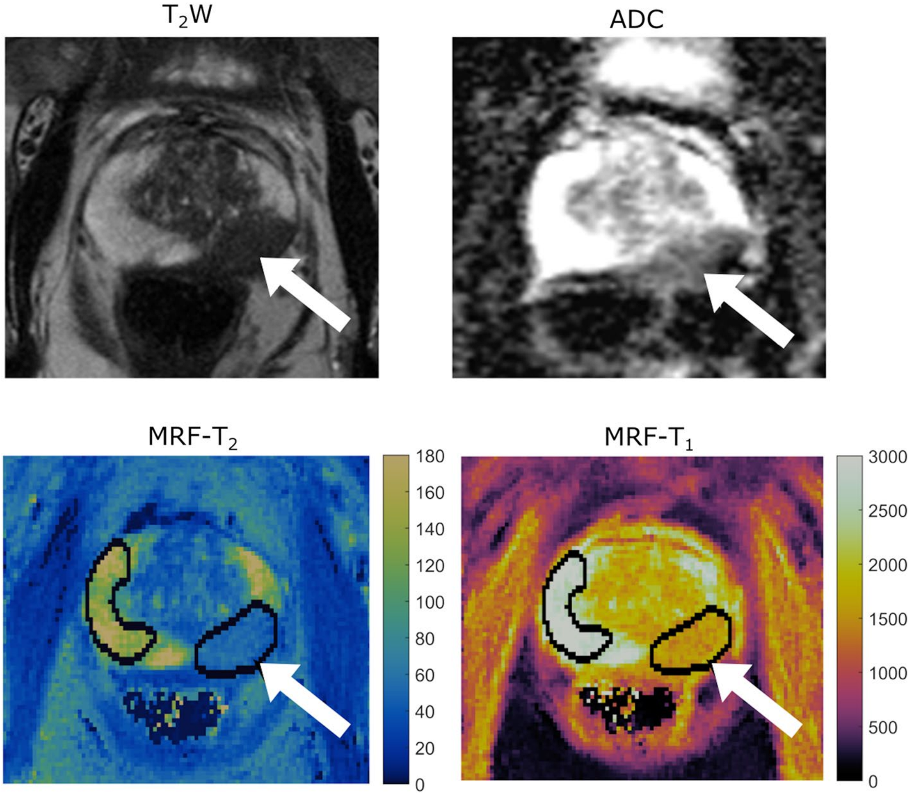

Fig. 3 Images and maps collected in a patient with prostate cancer (Gleason score 9) at 3 T. (top left) T_2-weighted axial image with a large hypointense cancer in the PZ (white thick arrow). (top right) The cancer demonstrates a lower diffusion coefficient on the Apparent Diffusion Coefficient (ADC) map. (bottom row) MRF-derived T_2 and T_1 maps, respectively. The cancer is marked on these maps by an ROI with a black border denoted again by the white arrow, and the normal-appearing PZ ROI marked with the simple black border

in a total of 140 patients at 3 T. Suspicious lesions were biopsied using either a standard 12-core TRUS approach or systematic biopsy plus cognitively targeted biopsy. All three quantitative tissue properties (T_1, T_2, and ADC) were significantly lower in cancer than in normal-appearing PZ tissue, and using all three of these metrics together provided an AUC of 0.99 to distinguish cancer from healthy tissue. This result was somewhat surprising, as T_1 had not previously been considered a property that changes in the presence of prostate cancer. Most interestingly, using T_2 and ADC, low-grade cancers could be distinguished from intermediate- and high-grade cancers with an AUC of 0.83. This finding suggests that MRF may be used to distinguish aggressiveness, and potentially indicates which patients may be followed up with active surveillance alone. Additionally, while T_1 and ADC could be used together to discriminate normal PZ tissue from prostatitis (AUC of 0.99), it was not possible to clearly separate cancer from prostatitis in the PZ using any combination of the quantitative parameters, likely because of the small sample size and small subset undergoing targeted biopsy.

In a follow-up study, 89 patients undergoing targeted biopsy (cognitive targeting with TRUS or in-bore MRI-guided biopsy) were recruited to be scanned with MRF at 3 T [14]. Quantitative differences between clinically significant cancers (Gleason score 3 + 4 = 7 and above), clinically insignificant cancers (Gleason 3 + 3 = 6), non-cancers (prostatitis and biopsy-proven normal prostate tissue) and clinically insignificant lesions (combined group of Gleason 6 cancers, prostatitis and negative biopsies) were evaluated. Example images from this study are shown in Fig. 4. This study confirmed that T_1 with ADC could be used to distinguish cancers from negative biopsies (AUC of 0.83) as well as non-cancers (AUC of 0.80), and T_2 and ADC could be used to distinguish clinically significant cancers (Gleason score 3 + 4 = 7 and above) from clinically insignificant

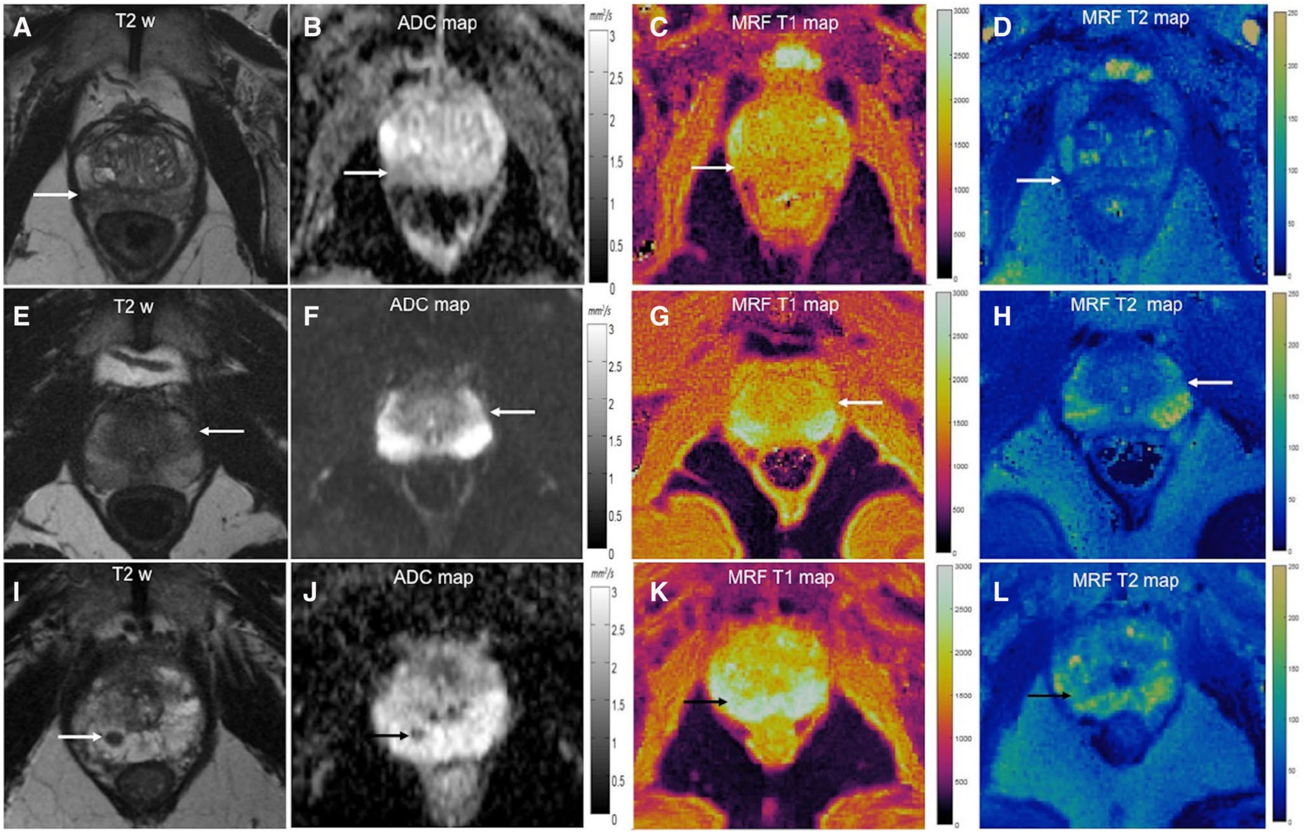

Fig. 4 Comparison of ADC, T_1 and T_2 values for targeted biopsy-proven prostate cancer (**A**–**D**), prostatitis (**E**–**H**) and benign prostatic tissue (**I**–**L**) collected at 3 T. Prostate cancer: T2w image (**A**) shows focal dark lesion against diffuse dark background signal in right peripheral zone with ADC of 0.87×10^{-3} mm^2/s (**B**). T_1 and T_2 values were 1560 ms and 42 ms respectively. Prostatitis: T2w (**E**) shows a wedge-shaped mildly dark lesion in left peripheral zone with ADC of 0.87×10^{-3} mm^2/s (**F**). T_1 and T_2 values were higher than cancer at 1770 ms and 83 ms respectively. Benign prostatic tissue: T2w (I) shows a focal lesion in right apical peripheral zone with ADC of 0.82×10^{-3} mm^2/s. Based on suspicious morphology on clinical MRI, biopsy was performed which revealed benign prostatic tissue. T_1 and T_2 values were higher than cancer at 2310 ms and 73 ms respectively. Figure reproduced from A. Panda et al., "Targeted Biopsy Validation of Peripheral Zone Prostate Cancer Characterization With Magnetic Resonance Fingerprinting and Diffusion Mapping," *Invest. Radiol.*, p. 1, 2019, https://doi.org/10.1097/rli.0000000000000569. with permission from Wolters Kluwer Health, Inc

(Gleason 3 + 3 = 6) cancers (AUC of 0.91), non-cancers (0.86), and clinically insignificant lesions (0.86). It was also possible to distinguish cancers from prostatitis (0.71 using T_2 and 0.79 with ADC), although the cut-offs used for this differentiation were more complicated. Both T_1 and T_2 were found to be significantly different between cancers and non-cancers, and these metrics provided information complementary to ADC when differentiating cancers from non-cancers. In this study, T_1 values of 1720 to 1730 ms, T_2 values of 52 to 60 ms and ADC values of 0.75 to 0.78×10^{-3} mm^2/s provided the best discriminatory performance between clinically significant cancers and non-cancers (see Fig. 5). While promising, one limitation of this study is that the diagnostic performance of these cutoff values was not validated in another cohort.

In comparison to lesions in the PZ, TZ cancers are more challenging to detect and characterize due to their location in a visually heterogeneous portion of the gland and similarities in appearance with benign nodules on T_2-weighted imaging. In [15], 67 men with 75 TZ lesions underwent MRI scans at 3 T including MRF, ADC mapping, and T_2-weighted imaging. As in the studies involving PZ lesions, areas of suspicion were identified in the T_2-weighted images, and quantitative T_1, T_2, and ADC values were measured over these areas. Figure 6 shows several example maps acquired in this study. The pathology of the lesions was determined via cognitively targeted TRUS biopsy ($N = 15$) and in-bore MRI-guided biopsy ($N = 60$). A combination of T_1 and ADC provided the best separation between prostate cancer and non-cancers (AUC of 0.94) and clinically significant prostate cancer and clinically insignificant TZ lesions (0.81). MRF-derived T_1 was also able to differentiate PI-RADS v2 category 3 non-cancers from cancers (AUC of 0.79). MRF-derived T_1 values of 1500 to 1510 ms and ADC values of 0.66 to 0.70×10^{-3} mm^2/s provided the best discriminatory performance for TZ lesions (see Fig. 7). Again $T_1 = 1500$ ms and ADC of 0.65×10^{-3} mm^2/s could be used as practical clinical cutoffs, although these have yet to be validated in another cohort.

Other studies have confirmed the findings that PZ and TZ T_1 and T_2 values measured with MRF are lower in cancer than in healthy prostate [92, 93], where the measured values are similar to those initially reported. Upon contrast administration, both the measured T_1 and T_2 have been shown to be reduced, although the reduction in both was lower in prostate cancer than in normal TZ and the reduction in T_1 lower in prostate cancer than in normal PZ. Small studies have reported excellent cross-system reproducibility of prostate MRF-based measurements at both 1.5 and 3 T in phantoms and healthy subjects [17], with similar values reported as those in [13, 14]. The ease of use as well as the repeatability and reproducibility of prostate MRF measurements has been explored in a small study performed over three different institutions (UHCMC, Brigham Women's, and DASA) with excellent results, indicating that this technique could indeed be generally deployed for clinical prostate assessment [16]. Additional studies with larger groups of men at more institutions are warranted to confirm the suggestion

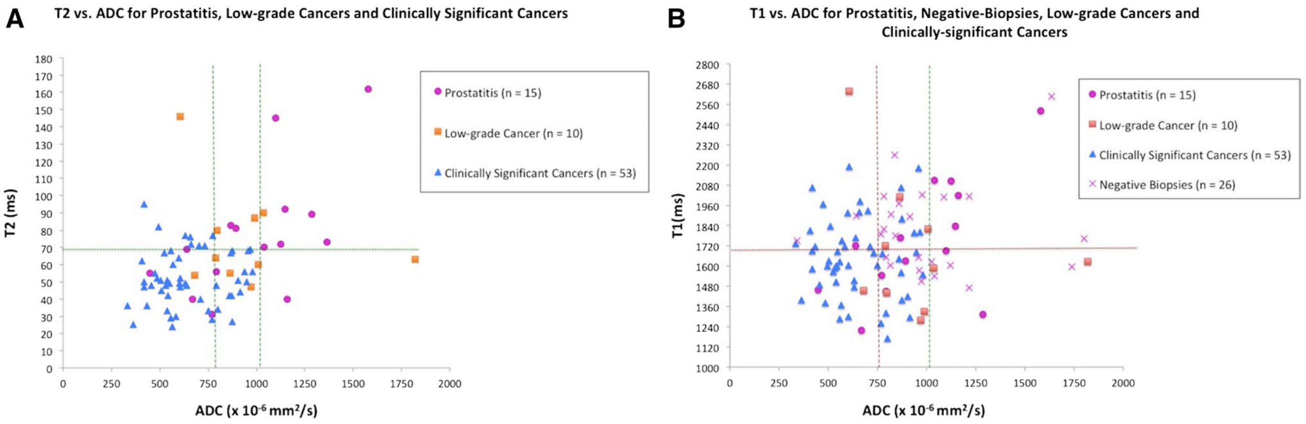

Fig. 5 Quantitative characterization with combined MRF-relaxometry and ADC mapping at 3 T. **a** Scatterplot of T_2 versus ADC for prostatitis ($n = 15$), low-grade cancers ($n = 10$) and clinically significant cancers ($n = 53$). ADC value of 1.04×10^{-3} mm^2/s is sensitive but not specific for differentiating all cancers from prostatitis (right vertical line). ADC value of 0.78×10^{-3} mm^2/s (left vertical line) is the best cut-off for differentiating clinically significant cancers from low-grade cancers and prostatitis. In the ADC overlap zone (between two vertical lines), a $T_2 \leq 68$ ms is additionally helpful in differentiating cancers from prostatitis (horizontal line). **b** Scatterplot of T_1 versus ADC for non-cancers including prostatitis ($n = 15$), negative biopsies ($n = 26$), low-grade cancers ($n = 10$) and clinically significant cancers ($n = 53$). ADC values of 0.75×10^{-3} mm^2/s followed by T_1 of 1720 ms are the best cut-offs for differentiating cancers from non-cancers (horizontal line). In the ADC overlap zone (between vertical lines), while five clinically significant cancers had $T_1 > 1720$ ms, they also had $T_2 \leq 68$ ms. Figure reproduced from A. Panda et al., "Targeted Biopsy Validation of Peripheral Zone Prostate Cancer Characterization With Magnetic Resonance Fingerprinting and Diffusion Mapping," *Invest. Radiol.*, p. 1, 2019, https://doi.org/10.1097/rli.0000000000000569. with permission from Wolters Kluwer Health, Inc

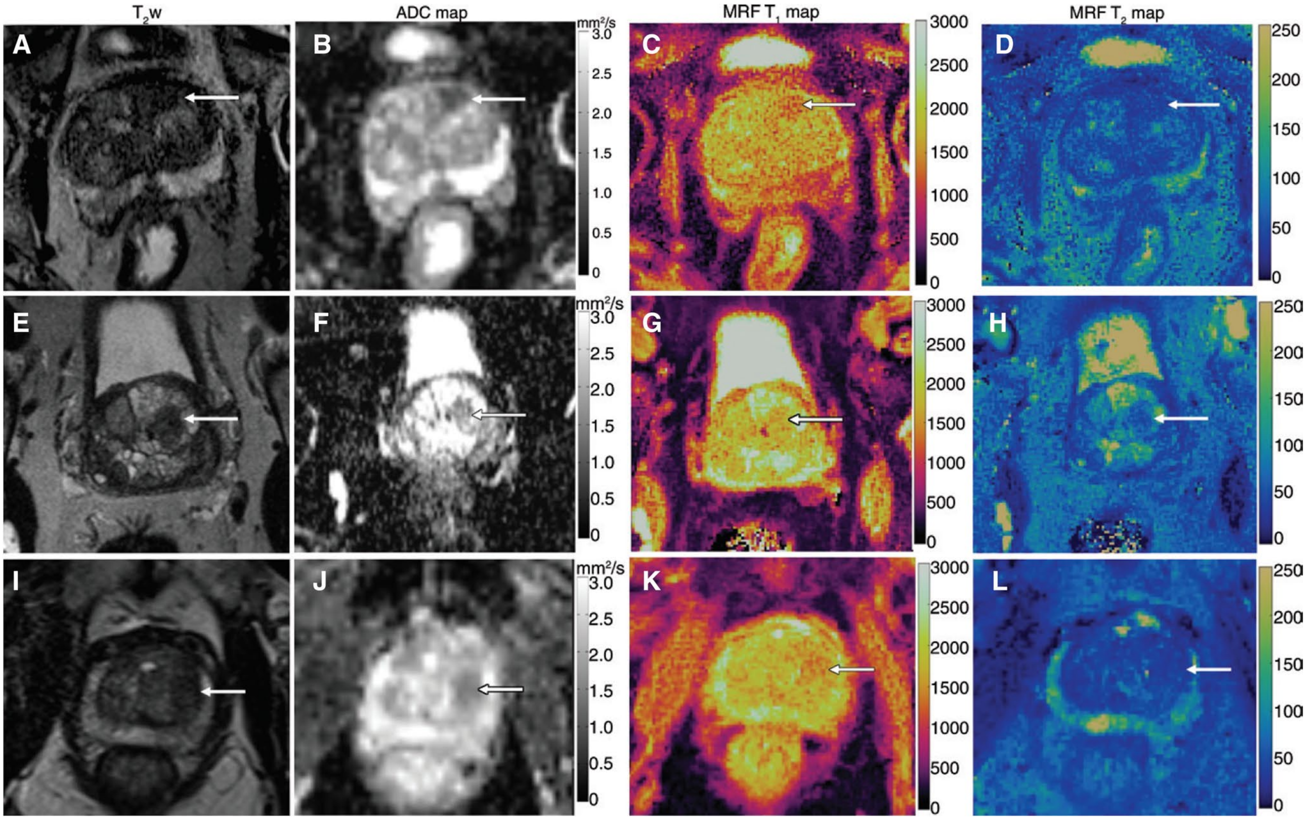

Fig. 6 Comparison of images from (left to right) axial T_2-weighted MRI, apparent diffusion coefficient (ADC) mapping, and T_1 and T_2 MR fingerprinting mapping for targeted biopsy-proven prostate cancer, prostatitis, and a benign prostatic hyperplasia (BPH) nodule all collected at 3 T. **A**–**D** Biopsy-proven prostate cancer (arrow). Mean T_1, T_2, and ADC were 1450 ms, 43 ms, and 0.51×10^{-3} mm²/s, respectively. **E**–**H** Biopsy-proven prostatitis (arrow). Mean T_1, T_2, and ADC were 1615 ms, 63 ms, and 0.83×10^{-3} mm²/s, respectively. **I**–**L**, For the BPH nodule (arrow), mean T_1, T_2, and ADC were 1600 ms, 43 ms, and $0.\ 87\times10^{-3}$ mm²/sec, respectively. Note the difference in T_1 relaxation times between transition zone cancer and noncancers despite the lesions having similar hypointense signal intensity on T_2-weighted images. Figure reproduced from A. Panda et al., "MR Fingerprinting and ADC Mapping for Characterization of Lesions in Transition Zone of the Prostate Gland," Radiology. 2019; 292:685–694, permission pending

that MRF-based measurements, coupled with ADC, could be used as a replacement for biopsy when the tissue can be definitively characterized using these quantitative metrics.

Another potential use of MRF beyond clinical tissue characterization is to better understand what histological changes drive T_1 and T_2 differences in various tissue states. In an intriguing article, areas of healthy tissue, prostatitis and cancer were identified in whole mount prostate specimens from men who were scanned with prostate MRF and then underwent prostatectomy, and the relative ratios of epithelium, lumen, and stroma were calculated these regions [92]. It was observed that: (1) the measured T_1 and T_2 values were negatively correlated with the ratio of epithelium, (2) the T_1 increased with increasing stroma in prostate cancer but decreased with increasing stroma in prostatitis, (3) the T_2 increased with increasing ratios of lumen in both prostate cancer and prostatitis. Given these associations, it may be possible to tailor the MRF sequence to specifically measure these differences in tissue components, thereby improving the precision and thus the discriminatory power of MRF. Work by Deshmane, et al. [19] has suggested that different tissue compartments in the brain can be assessed using MRF measurements, and such an approach may be valuable to pursue in prostate MRF as well. Moreover, it is known that a small number of cancers are missed on conventional MRI. With careful histological and quantitative analysis, it may be possible to determine if these missed cancers can be better detected quantitatively.

Future developments in prostate MRF

The most obvious next challenges in prostate MRF are the need to improve spatial resolution and scan times. The clinical studies described above used a 2D MRF implementation to collect T_1 and T_2 maps with an in-plane spatial resolution of $1\times1\text{mm}^2$ and a slice thickness of 5 mm. Compared to the resolution of clinical T_2-weighted images which are used to

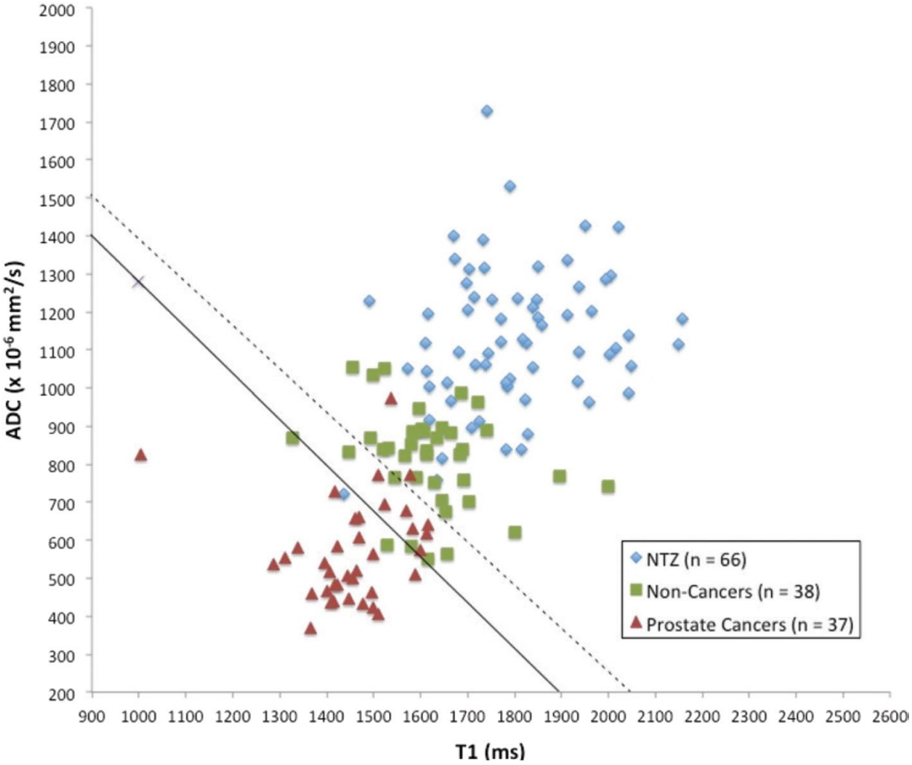

Fig. 7 Scatterplot of apparent diffusion coefficient (ADC) versus T_1 for normal transition zone (NTZ) ($n=66$), biopsy-proven noncancers ($n=38$), and prostate cancers ($n=37$) shows that cancers are well separated from biopsy-proven noncancers and NTZ in a quantitative space. Regions defined by the optimal model are denoted by the solid line (prostate cancers vs noncancers) and the dashed line (prostate cancers vs NTZ). Figure reproduced from A. Panda et al., "MR Fingerprinting and ADC Mapping for Characterization of Lesions in Transition Zone of the Prostate Gland," Radiology. 2019; 292:685–694, permission pending

detect prostate cancer, generally $0.6 \times 0.6 \text{mm}^2$ with a 3 mm slice thickness, the spatial resolution of these MRF-based tissue property maps is significantly lower. This lower resolution precludes the use of current MRF implementations for lesion detection. Moreover, the data acquisition times reported have been relatively long due to the need to capture each 2D slice independently in a scan lasting 39 to 50 s. A high-resolution ($0.6 \times 0.6 \times 3 \text{mm}^3$) 3D prostate MRF acquisition scheme which could be explored for lesion detection has been developed with a data acquisition time of 3 min and 48 s [93]. This resolution is identical to that used in conventional T_2-weighted imaging of the prostate, and the scan time is not substantially longer than multi-slice 2D MRF. While only a small number of lesions were assessed and those that were examined were not separated by their location in the prostate, initial results in 90 men suspected of having prostate cancer have been in step with prior studies [14, 15]. The development of a relatively rapid high-resolution 3D prostate MRF approach may eventually eliminate the need for a separate high-resolution T_2-weighted scan, as a synthetic image could be generated from the T_2 map itself, or lesions could be directly detected using the MRF-based maps. It is anticipated that future prostate MRF studies will adopt high-resolution 3D approaches due to these benefits.

Another challenge is that the current implementation of prostate MRF enables the simultaneous quantification of T_1 and T_2, but not ADC, which has been measured in a separate scan for the clinical studies described above. With such an approach, the T_1 and T_2 maps are inherently co-registered, but the ADC map may not be perfectly aligned with the MRF-based maps. Indeed, as the diffusion images are collected with EPI and more susceptible to distortion than the MRF-based maps, a potentially error-inducing registration step is required. An MRF implementation which measures T_1 and T_2 as well as ADC would be far preferable to the use of two different scans. While it is theoretically possible to measure additional tissue properties along with T_1 and T_2 with MRF, including but not limited to perfusion [96, 97], fat fraction [98–101], and diffusion [102], it is quite challenging to measure both diffusion and T_2 at the same time with MRF. Implementations of MRF which including diffusion measurements have broken the acquisition up into two portions, one of which is used to assess T_1 and T_2, and one which is used to measure T_1 and ADC. However, even this approach has not been widely adopted due to the long scan times needed to acquire information about all three tissue properties, and the low signal levels which result from both T_2- and diffusion-weighting. Other groups have reported the ability to measure all three properties [103], but this approach has not yet been tested in the prostate. Until an efficient and accurate combined T_1/T_2/ADC MRF acquisition and reconstruction scheme specific to the prostate is developed, a separately acquired conventional ADC map must be used to assess the diffusion characteristics of lesions. Across all these technical challenges, multi-institutional and multi-vendor validated implementations of the technique would allow more routine scanning at non-expert sites, and robust comparisons across patients and cohorts.

Finally, the significant and clinically-relevant challenge of definitively distinguishing various pathologies in the prostate persists, even when using the quantitative measurements of three different tissue properties. For example, while it may be possible to distinguish cancer from prostatitis in some cases, a robust approach to characterize these different tissues would be of great clinical interest. The difficulty may lie in the fact that the properties of healthy tissue and pathological tissue are similar (i.e., similar T_1, T_2, and ADC), and an additional tissue property may be needed to enable their discrimination. Another possibility is that the variance in the measurements of these tissue properties is currently too large; more precise measurements using improved MRF sequences may be helpful. Sub-characterization of Category 3 lesions in the PIRADs 2.1 system into high and low risk groups is another major open problem in that would have high clinical impact. MRF of metastatic lesions (for example in osseous structures) and measuring their response to treatment is another major goal of future clinical work.

Conclusion

Prostate MRF is an evolving technology for prostate imaging and tissue property mapping. Together with ADC maps, the T_1 and T_2 maps derived using MRF have been used to discriminate cancers from non-cancers and healthy prostate tissue in both the peripheral and transition zones. While potential improvements to the MRF acquisition and reconstruction are under investigation, including the acquisition of higher resolution or 3D maps or the addition of ADC to the measured tissue properties, initial MRF results suggest that this technique may become a useful tool for the characterization of prostate tissue.

Acknowledgements Siemens Healthineers, National Science Foundation/Chemical, Bioengineering, Environmental and Transport Systems 1553441, National Institutes of Health/ National Cancer Institute R01CA208236, National Institutes of Health/National Cancer Institute R37CA263583

Author contributions W-CL: Data collection and analysis, Literature review, Drafting of manuscript, Critical revision. AP: Drafting of manuscript, Critical revision. YJ: Drafting of manuscript, Critical revision. JA: Literature review, Drafting of manuscript, Critical revision. VG: Literature review, Drafting of manuscript, Critical revision. NS: Literature review, Drafting of manuscript, Critical revision.

Funding This study was funded by Siemens Healthineers, National Science Foundation/Chemical, Bioengineering, Environmental and Transport Systems (Grant number 1553441), National Institutes of Health (Grant numbers R01CA208236, R37CA263583, F30CA23935, T32GM007250).

Declarations

Conflict of interest Authors Lo, Panda, Jiang, Ahad, Gulani, and Seiberlich have received research grants from Siemens Healthineers, and authors Jiang, Gulani, and Seiberlich have received royalties from Siemens Healthineers for MRF. Author Lo is currently an employee of Siemens Healthineers.

Ethical approval All procedures performed in studies involving human participants were in accordance with the ethical standards of the institutional and/or national research committee and with the 1964 Helsinki declaration and its later amendments or comparable ethical standards. This article does not contain any studies with animals performed by any of the authors.

Informed consent Informed consent was obtained from all individual participants included in the study.

References

1. Walker SM, Choyke PL, Turkbey B (2020) What you need to know before reading multiparametric MRI for prostate cancer. AJR Am J Roentgenol 214(6):1211–1219. https://doi.org/10.2214/AJR.19.22751
2. Stabile A et al (2020) Multiparametric MRI for prostate cancer diagnosis: current status and future directions. Nat Rev Urol 17(1):41–61. https://doi.org/10.1038/s41585-019-0212-4
3. Giganti F et al (2019) The evolution of MRI of the prostate: the past, the present, and the future. AJR Am J Roentgenol 213(2):384–396. https://doi.org/10.2214/AJR.18.20796
4. Verma S, Choyke PL, Eberhardt SC et al (2017) The current state of mr imaging–targeted biopsy techniques for detection of prostate cancer. Radiology 285(2):343–356. https://doi.org/10.1148/radiol.2017161684
5. Purysko AS et al (2020) PI-RADS Version 2.1: a critical review, from the AJR special series on radiology reporting and data systems. Am J Roentgenol 216(1):20–32. https://doi.org/10.2214/AJR.20.24495
6. Rosenkrantz AB, Taneja SS (2014) Radiologist, be aware: ten pitfalls that confound the interpretation of multiparametric prostate MRI. AJR Am J Roentgenol 202(1):109–120. https://doi.org/10.2214/AJR.13.10699
7. Chatterjee A, Watson G, Myint E, Sved P, McEntee M, Bourne R (2015) Changes in epithelium, stroma, and lumen space correlate more strongly with gleason pattern and are stronger predictors of prostate adc changes than cellularity metrics. Radiology 277(3):751–762. https://doi.org/10.1148/radiol.2015142414
8. Dickinson L et al (2011) Magnetic resonance imaging for the detection, localisation, and characterisation of prostate cancer: recommendations from a European consensus meeting. Eur Urol 59(4):477–494. https://doi.org/10.1016/j.eururo.2010.12.009
9. Heye T et al (2013) Reproducibility of dynamic contrast-enhanced MR imaging. Part I. Perfusion characteristics in the female pelvis by using multiple computer-aided diagnosis perfusion analysis solutions. Radiology 266(3):801–811. https://doi.org/10.1148/radiol.12120278
10. Heye T et al (2013) Reproducibility of dynamic contrast-enhanced MR imaging. Part II. Comparison of intra- and inter-observer variability with manual region of interest placement versus semiautomatic lesion segmentation and histogram analysis. Radiology 266(3):812–821. https://doi.org/10.1148/radiol.12120255

11. Ma D et al (2013) Magnetic resonance fingerprinting. (1). Nature 495(7440):187–192. https://doi.org/10.1038/nature11971
12. Jiang Y, Ma D, Seiberlich N, Gulani V, Griswold MA (2015) MR fingerprinting using fast imaging with steady state precession (FISP) with spiral readout. Magn Reson Med 74(6):1621–1631. https://doi.org/10.1002/mrm.25559
13. Yu AC et al (2017) Development of a combined MR fingerprinting and diffusion examination for prostate cancer. Radiology 283(3):729–738. https://doi.org/10.1148/radiol.2017161599
14. Panda A et al (2019) Targeted biopsy validation of peripheral zone prostate cancer characterization with magnetic resonance fingerprinting and diffusion mapping. Invest Radiol. https://doi.org/10.1097/rli.0000000000000569
15. Panda A et al (2019) MR fingerprinting and ADC mapping for characterization of lesions in transition zone of the prostate gland. Radiology 292:685–694
16. Lo WC et al. (2018) Multicenter repeatability and reproducibility of MR fingerprinting. In: Proc Intl Soc Mag Reson Med, p 4503
17. Sushentsev N, Kaggie JD, Slough RA, Carmo B (2021) T Barrett (2021) Reproducibility of magnetic resonance fingerprinting-based T1 mapping of the healthy prostate at 1.5 and 3.0 T: a proof-of-concept study. PLoS ONE 16(1):245970. https://doi.org/10.1371/journal.pone.0245970
18. Tang S, Fernandez-Granda C, Lannuzel S, Bernstein B, Lattanzi R, Cloos M, Knoll F, Assländer J (2018) Multicompartment magnetic resonance fingerprinting. Inverse Probl 34(9):094005. https://doi.org/10.1088/1361-6420/aad1c3 (**Epub 2018 Jul 24. PMID: 30880863; PMCID: PMC6415771**)
19. Deshmane A, McGivney DF, Ma D, Jiang Y, Badve C, Gulani V, Seiberlich N, Griswold MA (2019) Partial volume mapping using magnetic resonance fingerprinting. NMR Biomed 32(5):e4082. https://doi.org/10.1002/nbm.4082 (**Epub 2019 Mar 1. PMID: 30821878**)
20. Hermann I, Martínez-Heras E, Rieger B, Schmidt R, Golla AK, Hong JS, Lee WK, Yu-Te W, Nagtegaal M, Solana E, Llufriu S, Gass A, Schad LR, Weingärtner S, Zöllner FG (2021) Accelerated white matter lesion analysis based on simultaneous T1 and T2$*$ quantification using magnetic resonance fingerprinting and deep learning. Magn Reson Med 86(1):471–486. https://doi.org/10.1002/mrm.28688 (**Epub 2021 Feb 5 PMID: 33547656**)
21. Hricak H et al (1987) MR imaging of the prostate gland: normal anatomy. AJR Am J Roentgenol 148(1):51–58. https://doi.org/10.2214/ajr.148.1.51
22. Barentsz JO et al (2012) ESUR prostate MR guidelines 2012. Eur Radiol 22(4):746–757. https://doi.org/10.1007/s00330-011-2377-y
23. Weinreb JC et al (2016) PI-RADS prostate imaging—reporting and data system: 2015, Version 2. Eur Urol 69(1):16–40. https://doi.org/10.1016/j.eururo.2015.08.052
24. Wang L, Mazaheri Y, Zhang J, Ishill NM, Kuroiwa K, Hricak H (2008) Assessment of biologic aggressiveness of prostate cancer: correlation of MR signal intensity with Gleason grade after radical prostatectomy. Radiology 246(1):168–176. https://doi.org/10.1148/radiol.2461070057
25. Somford DM, Fütterer JJ, Hambrock T, Barentsz JO (2008) Diffusion and perfusion MR imaging of the prostate. Magn Reson Imaging Clin N Am 16(4):685–695. https://doi.org/10.1016/j.mric.2008.07.002
26. Kim CK, Park BK, Kim B (2010) High-b-value diffusion-weighted imaging at 3 T to detect prostate cancer: comparisons between b values of 1,000 and 2,000 s/mm2. AJR Am J Roentgenol 194(1):W33–W37. https://doi.org/10.2214/AJR.09.3004
27. Hambrock T et al (2011) Relationship between apparent diffusion coefficients at 3.0-T MR imaging and Gleason grade in peripheral zone prostate cancer. Radiology 259(2):453–461. https://doi.org/10.1148/radiol.11091409
28. Wu L-M, Xu J-R, Ye Y-Q, Lu Q, Hu J-N (2012) The clinical value of diffusion-weighted imaging in combination with T2-weighted imaging in diagnosing prostate carcinoma: a systematic review and meta-analysis. AJR Am J Roentgenol 199(1):103–110. https://doi.org/10.2214/AJR.11.7634
29. Il Jung S, Donati OF, Vargas HA, Goldman D, Hricak H, Akin O (2013) Transition zone prostate cancer: incremental value of diffusion-weighted endorectal MR imaging in tumor detection and assessment of aggressiveness. Radiology 269(2):493–503. https://doi.org/10.1148/radiol.13130029
30. Hara N, Okuizumi M, Koike H, Kawaguchi M, Bilim V (2005) Dynamic contrast-enhanced magnetic resonance imaging (DCE-MRI) is a useful modality for the precise detection and staging of early prostate cancer. Prostate 62(2):140–147. https://doi.org/10.1002/pros.20124
31. Heye T, Merkle EM, Reiner CS, Davenport MS, Horvath JJ, Feuerlein S, Breault SR, Gall P, Bashir MR, Dale BM, Kiraly AP, Boll DT (2013) Reproducibility of dynamic contrast-enhanced MR imaging. Part II. Comparison of intra- and interobserver variability with manual region of interestplacement versus semiautomatic lesion segmentation and histogram analysis. Radiology 3:812–821
32. Lovegrove CE et al (2018) Prostate imaging features that indicate benign or malignant pathology on biopsy. Transl Androl Urol 7(Suppl 4):S420–S435. https://doi.org/10.21037/tau.2018.07.06
33. Purysko AS, Herts BR (2012) Prostate MRI: the hemorrhage exclusion sign. J Urol 188(5):1946–1947. https://doi.org/10.1016/j.juro.2012.08.058
34. Rosenkrantz AB et al (2016) Interobserver reproducibility of the PI-RADS Version 2 lexicon: a multicenter study of six experienced prostate radiologists. Radiology 280(3):793–804. https://doi.org/10.1148/radiol.2016152542
35. Westphalen AC et al (2020) Variability of the positive predictive value of PI-RADS for prostate MRI across 26 centers: experience of the society of abdominal radiology prostate cancer disease-focused panel. Radiology 296(1):76–84. https://doi.org/10.1148/radiol.2020190646
36. Gaziev G et al (2016) Defining the learning curve for multiparametric magnetic resonance imaging (MRI) of the prostate using MRI-transrectal ultrasonography (TRUS) fusion-guided transperineal prostate biopsies as a validation tool. BJU Int 117(1):80–86. https://doi.org/10.1111/bju.12892
37. Akin O, Riedl CC, Ishill NM, Moskowitz CS, Zhang J, Hricak H (2010) Interactive dedicated training curriculum improves accuracy in the interpretation of MR imaging of prostate cancer. Eur Radiol 20(4):995–1002. https://doi.org/10.1007/s00330-009-1625-x
38. Lee CH (2019) Quantitative T2-mapping using MRI for detection of prostate malignancy: a systematic review of the literature. Acta Radiol 60(9):1181–1189. https://doi.org/10.1177/0284185118820058 (**Epub 2019 Jan 8 PMID: 30621443**)
39. Mai J et al (2019) T2 mapping in prostate cancer. Invest Radiol 54(3):146–152. https://doi.org/10.1097/RLI.0000000000000520
40. Jambor I, Pesola M, Merisaari H et al (2016) Relaxation along fictitious field, diffusion-weighted imaging, and T2 mapping of prostate cancer: prediction of cancer aggressiveness. Magn Reson Med 75(5):2130–2140
41. Liu W, Turkbey B, Sénégas J, Remmele S, Xu S, Kruecker J, Bernardo M, Wood BJ, Pinto PA, Choyke PL (2011) Accelerated T2 mapping for characterization of prostate cancer. Magn Reson Med 65(5):1400–1406. https://doi.org/10.1002/mrm.22874
42. Yamauchi FI, Penzkofer T, Fedorov A et al (2015) Prostate cancer discrimination in the peripheral zone with a reduced field-of-view T(2)-mapping MRI sequence. Magn Reson Imaging 33(5):525–530

43. Bonekamp D, Jacobs MA, El-Khouli R, Stoianovici D, Macura KJ (2011) Advancements in MR imaging of the prostate: from diagnosis to interventions. Radiographics 31(3):677–703. https://doi.org/10.1148/rg.313105139
44. Boesen L, Chabanova E, Lgager V, Balslev I, Thomsen HS (2015) Apparent diffusion coefficient ratio correlates significantly with prostate cancer Gleason score at final pathology. J Magn Reson Imaging 42(2):446–453
45. Hoang Dinh A et al (2015) Characterization of prostate cancer using T2 mapping at 3T: a multi-scanner study. Diagn Interv Imaging 96(4):365–372. https://doi.org/10.1016/j.diii.2014.11.016
46. Boesen L, Chabanova E, Løgager V, Balslev I, Thomsen HS (2015) Apparent diffusion coefficient ratio correlates significantly with prostate cancer gleason score at final pathology. J Magn Reson Imaging 42(2):446–453. https://doi.org/10.1002/jmri.24801
47. Kim CK, Park BK, Han JJ, Kang TW, Lee HM (2007) Diffusion-weighted imaging of the prostate at 3 T for differentiation of malignant and benign tissue in transition and peripheral zones: preliminary results. J Comput Assist Tomogr 31(3):449–454. https://doi.org/10.1097/01.rct.0000243456.00437.59
48. Gibbs P, Liney GP, Pickles MD, Zelhof B, Rodrigues G, Turnbull LW (2009) Correlation of ADC and T2 measurements with cell density in prostate cancer at 3.0 Tesla. Invest Radiol 44(9):572–576. https://doi.org/10.1097/RLI.0b013e3181b4c10e
49. Nagel KNA et al (2013) Differentiation of prostatitis and prostate cancer by using diffusion-weighted MR imaging and MR-guided biopsy at 3 T. Radiology 267(1):164–172. https://doi.org/10.1148/radiol.12111683
50. Simpkin CJ, Morgan VA, Giles SL, Riches SF, Parker C, Souza NM (2013) Relationship between T2 relaxation and apparent diffusion coefficient in malignant and non-malignant prostate regions and the effect of peripheral zone fractional volume. Br J Radiol 86(1024):20120469. https://doi.org/10.1259/bjr.20120469
51. Chatterjee A, Devaraj A, Mathew M, Szasz T, Antic T, Karczmar GS, Oto A (2019) Performance of T2 maps in the detection of prostate cancer. Acad Radiol 26(1):15–21. https://doi.org/10.1016/j.acra.2018.04.005
52. Baur ADJ et al (2020) Evaluation of T1 relaxation time in prostate cancer and benign prostate tissue using a Modified Look-Locker inversion recovery sequence. Sci Rep 10(1):3121. https://doi.org/10.1038/s41598-020-59942-z
53. Cui Y, Han S, Liu M, Wu PY, Zhang W, Zhang J, Li C, Chen M (2020) Diagnosis and grading of prostate cancer by relaxation maps from synthetic MRI. J Magn Reson Imaging 52(2):552–564. https://doi.org/10.1002/jmri.27075 (**Epub 2020 Feb 6 PMID: 32027071**)
54. Fedorov A, Penzkofer T, Hirsch MS et al (2015) The role of pathology correlation approach in prostate cancer index lesion detection and quantitative analysis with multiparametric MRI. Acad Radiol 22(5):548–555
55. Sabouri S, Chang SD, Savdie R, Zhang J, Jones EC, Goldenberg SL, Black PC, Kozlowski P (2017) Luminal water imaging: a new MR imaging T2 mapping technique for prostate cancer diagnosis. Radiology 284(2):451–459. https://doi.org/10.1148/radiol.2017161687
56. Chatterjee A, He D, Fan X, Antic T, Jiang Y, Eggener S, Karczmar GS, Oto A (2019) Diagnosis of prostate cancer by use of MRI-derived quantitative risk maps: a feasibility study. AJR Am J Roentgenol 213(2):W66–W75. https://doi.org/10.2214/AJR.18.20702 (**Epub 2019 Apr 30 PMID: 31039019**)
57. Badve C et al (2015) Simultaneous T(1) and T(2) brain relaxometry in asymptomatic volunteers using magnetic resonance fingerprinting. Tomogr Ann Arbor Mich 1(2):136–144. https://doi.org/10.18383/j.tom.2015.00166
58. Badve C et al (2016) Magnetic resonance fingerprinting of adult brain tumors: initial experience. AJNR Am Neuroradiol 51(1):87–100. https://doi.org/10.1037/a0038432.Latino
59. Chen Y et al (2016) MR fingerprinting for rapid quantitative abdominal imaging. Radiology 279(1):278–286. https://doi.org/10.1148/radiol.2016152037
60. Hamilton JI et al (2017) MR fingerprinting for rapid quantification of myocardial T1, T2, and proton spin density. Magn Reson Med 77(4):C1. https://doi.org/10.1002/mrm.26668
61. Chen Y et al (2019) Three-dimensional MR fingerprinting for quantitative breast imaging. Radiology 290(1):33–40. https://doi.org/10.1148/radiol.2018180836
62. Panda A, Chen Y, Ropella-Panagis K, Ghodasara S, Stopchinski M, Seyfried N, Wright K, Seiberlich N, Griswold M, Gulani V (2019) Repeatability and reproducibility of 3D MR fingerprinting relaxometry measurements in normal breast tissue. J Magn Reson Imaging 50(4):1133–1143. https://doi.org/10.1002/jmri.26717 (**Epub 2019 Mar 20. PMID: 30892807; PMCID: PMC6750981**)
63. Hamilton JI, Jiang Y, Ma D, Lo WC, Gulani V, Griswold M, Seiberlich N (2018) Investigating and reducing the effects of confounding factors for robust T1 and T2 mapping with cardiac MR fingerprinting. Magn Reson Imaging 30(53):40–51
64. Kara D, Fan M, Hamilton J, Griswold M, Seiberlich N, Brown R (2019) Parameter map error due to normal noise and aliasing artifacts in MR fingerprinting. Magn Reson Med 81(5):3108–3123. https://doi.org/10.1002/mrm.27638 (**Epub 2019 Jan 23. PMID: 30671999; PMCID: PMC6414267**)
65. Lahiri A, Fessler JA, Hernandez-Garcia L (2020) Optimizing MRF-ASL scan design for precise quantification of brain hemodynamics using neural network regression. Magn Reson Med 83(6):1979–1991. https://doi.org/10.1002/mrm.28051 (**Epub 2019 Nov 21 PMID: 31751497**)
66. Jordan SP, Hu S, Rozada I, McGivney DF, Boyacioğlu R, Jacob DC, Huang S, Beverland M, Katzgraber HG, Troyer M, Griswold MA, Ma D (2021) Automated design of pulse sequences for magnetic resonance fingerprinting using physics-inspired optimization. Proc Natl Acad Sci USA 118(40):e2020516118. https://doi.org/10.1073/pnas.2020516118
67. Fang Z, Chen Y, Liu M, Xiang L, Zhang Q, Wang Q, Lin W, Shen D (2019) Deep learning for fast and spatially constrained tissue quantification from highly accelerated data in magnetic resonance fingerprinting. IEEE Trans Med Imaging 38(10):2364–2374. https://doi.org/10.1109/TMI.2019.2899328(Epub2019Feb13.PMID:30762540;PMCID:PMC6692257)
68. Cohen O, Rosen MS (2017) Algorithm comparison for schedule optimization in MR fingerprinting. Magn Reson Imaging 41:15–21. https://doi.org/10.1016/j.mri.2017.02.010 (**Epub 2017 Feb 24 PMID: 28238942**)
69. Fessler JA (2007) On NUFFT-based gridding for non-Cartesian MRI. J Magn Reson 188:191–195
70. Cao X, Liao C, Wang Z, Chen Y, Ye H, He H, Zhong J (2017) Robust sliding-window reconstruction for Accelerating the acquisition of MR fingerprinting. Magn Reson Med 78(4):1579–1588. https://doi.org/10.1002/mrm.26521 (**Epub 2016 Nov 7 PMID: 27851871**)
71. Liao C et al (2017) 3D MR fingerprinting with accelerated stack-of-spirals and hybrid sliding-window and GRAPPA reconstruction. Neuroimage 162:13–22. https://doi.org/10.1016/j.neuroimage.2017.08.030
72. Pierre EY, Ma D, Chen Y, Badve C, Griswold MA (2016) Multiscale reconstruction for MR fingerprinting. Magn Reson Med 75(6):2481–2492. https://doi.org/10.1002/mrm.25776

73. Mazor G, Weizman L, Tal A, Eldar YC (2018) Low-rank magnetic resonance fingerprinting. Med Phys. https://doi.org/10.1002/mp.13078
74. Koolstra K, Beenakker JM, Koken P, Webb A, Börnert P (2019) Cartesian MR fingerprinting in the eye at 7T using compressed sensing and matrix completion-based reconstructions. Magn Reson Med 81(4):2551–2565. https://doi.org/10.1002/mrm.27594
75. Assländer J, Cloos MA, Knoll F, Sodickson DK, Hennig J, Lattanzi R (2018) Low rank alternating direction method of multipliers reconstruction for MR fingerprinting. Magn Reson Med 79(1):83–96
76. Zhao B, Setsompop K, Adalsteinsson E, Gagoski B, Ye H, Ma D, Jiang Y, Ellen Grant P, Griswold MA, Wald LL (2018) Improved magnetic resonance fingerprinting reconstruction with low-rank and subspace modeling. Magn Reson Med 79(2):933–942
77. Lima da Cruz G, Bustin A, Jaubert O, Schneider T, Botnar RM, Prieto C (2019) Sparsity and locally low rank regularization for MR fingerprinting. Magn Reson Med 81(6):3530–3543. https://doi.org/10.1002/mrm.27665
78. Walsh DO, Gmitro AF, Marcellin MW (2000) Adaptive reconstruction of phased array MR imagery. Magn Reson Med 43:682–690
79. Huang F, Vijayakumar S, Li Y, Hertel S, Duensing GR (2008) A software channel compression technique for faster reconstruction with many channels. Magn Reson Imaging 26(1):133–141. https://doi.org/10.1016/j.mri.2007.04.010 (**Epub 2007 Jun 15 PMID: 17573223**)
80. Yang M, Ma D, Jiang Y, Hamilton J, Seiberlich N, Griswold MA, McGivney D (2018) Low rank approximation methods for MR fingerprinting with large scale dictionaries. Magn Reson Med 79(4):2392–2400. https://doi.org/10.1002/mrm.26867 (**Epub 2017 Aug 13. PMID: 28804918; PMCID: PMC5811391**)
81. Wang D, Ostenson J, Smith DS (2020) snapMRF: GPU-accelerated magnetic resonance fingerprinting dictionary generation and matching using extended phase graphs. Magn Reson Imaging 66:248–256. https://doi.org/10.1016/j.mri.2019.11.015 (**Epub 2019 Nov 15. PMID: 31740194; PMCID: PMC7031031**)
82. Ostenson J, Smith DS, Does MD, Damon BM (2020) Slice-selective extended phase graphs in gradient-crushed, transient-state free precession sequences: an application to MR fingerprinting. Magn Reson Med 84(6):3409–3422. https://doi.org/10.1002/mrm.28381 (**Epub 2020 Jul 22. PMID: 32697869; PMCID: PMC8485742**)
83. Hamilton JI, Seiberlich N (2020) Machine learning for rapid magnetic resonance fingerprinting tissue property quantification. Proc IEEE Inst Electr Electron Eng 108(1):69–85
84. Cauley SF, Setsompop K, Ma D, Jiang Y, Ye H, Adalsteinsson E, Griswold MA, Wald LL (2015) Fast group matching for MR fingerprinting reconstruction. Magn Reson Med 74(2):523–528. https://doi.org/10.1002/mrm.25439 (**Epub 2014 Aug 28. PMID: 25168690; PMCID: PMC4700821**)
85. Hoppe E, Körzdörfer G, Würfl T, Wetzl J, Lugauer F, Pfeuffer J, Maier A (2017) Deep learning for magnetic resonance fingerprinting: a new approach for predicting quantitative parameter values from time series. Stud Health Technol Inform 243:202–206
86. Cohen O, Zhu B, Rosen MS (2018) MR fingerprinting Deep RecOnstruction NEtwork (DRONE). Magn Reson Med 80(3):885–894
87. Song P, Eldar YC, Mazor G, Rodrigues MRD (2019) HYDRA: Hybrid deep magnetic resonance fingerprinting. Med Phys 46(11):4951–4969. https://doi.org/10.1002/mp.13727 (**Epub 2019 Sep 10 PMID: 31329307**)
88. Chen Y, Fang Z, Hung SC, Chang WT, Shen D, Lin W (2020) High-resolution 3D MR Fingerprinting using parallel imaging and deep learning. Neuroimage 206:116329. https://doi.org/10.1016/j.neuroimage.2019.116329 (**Epub 2019 Nov 2. PMID: 31689536; PMCID: PMC7136033**)
89. Liu H, van der Heide O, van den Berg CAT, Sbrizzi A (2021) Fast and accurate modeling of transient-state, gradient-spoiled sequences by recurrent neural networks. NMR Biomed 34(7):e4527. https://doi.org/10.1002/nbm.4527 (**Epub 2021 May 5. PMID: 33949718; PMCID: PMC8244023**)
90. Cao P, Cui D, Vardhanabhuti V, Hui ES (2020) Development of fast deep learning quantification for magnetic resonance fingerprinting in vivo. Magn Reson Imaging 70:81–90. https://doi.org/10.1016/j.mri.2020.03.009 (**Epub 2020 Apr 7 PMID: 32276007**)
91. Kim B, Schär M, Park H, Heo HY (2020) A deep learning approach for magnetization transfer contrast MR fingerprinting and chemical exchange saturation transfer imaging. Neuroimage 221:117165. https://doi.org/10.1016/j.neuroimage.2020.117165
92. Sushentsev N et al (2020) The effect of gadolinium-based contrast agent administration on magnetic resonance fingerprinting-based T(1) relaxometry in patients with prostate cancer. Sci Rep 10(1):20475. https://doi.org/10.1038/s41598-020-77331-4
93. Lee YS, Choi MH, Lee YJ, Han D, Kim D (2021) Magnetic resonance fingerprinting in prostate cancer before and after contrast enhancement. Br J Radiol 94:20210479
94. Shiradkar R, Panda A, Leo P, Janowczyk A, Farre X, Janaki N, Li L, Pahwa S, Mahran A, Buzzy C, Fu P, Elliott R, MacLennan G, Ponsky L, Gulani V, Madabhushi A (2021) T1 and T2 MR fingerprinting measurements of prostate cancer and prostatitis correlate with deep learning-derived estimates of epithelium, lumen, and stromal composition on corresponding whole mount histopathology. Eur Radiol 31(3):1336–1346. https://doi.org/10.1007/s00330-020-07214-9 (**Epub 2020 Sep 2. Erratum in: Eur Radiol. 2020 Sep 18;: PMID: 32876839; PMCID: PMC7882016**)
95. Han D, Choi MH, Lee YJ, Kim DH (2021) Feasibility of novel three-dimensional magnetic resonance fingerprinting of the prostate gland: phantom and clinical studies. Korean J Radiol. https://doi.org/10.3348/kjr.2020.1362 (**Epub ahead of print. PMID: 34047506**)
96. Wright KL, Jiang Y, Ma D, Noll DC, Griswold MA, Gulani V, Hernandez-Garcia L (2018) Estimation of perfusion properties with MR Fingerprinting Arterial Spin Labeling. Magn Reson Imaging 50:68–77. https://doi.org/10.1016/j.mri.2018.03.011
97. Su P, Fan H, Liu P, Li Y, Qiao Y, Hua J, Lin D, Jiang D, Pillai JJ, Hillis AE, Lu H (2020) MR fingerprinting ASL: sequence characterization and comparison with dynamic susceptibility contrast (DSC) MRI. NMR Biomed 33(1):e4202. https://doi.org/10.1002/nbm.4202 (**Epub 2019 Nov 4. PMID: 31682305; PMCID: PMC7229700.**)
98. Cencini M, Biagi L, Kaggie JD, Schulte RF, Tosetti M, Buonincontri G (2019) Magnetic resonance fingerprinting with dictionary-based fat and water separation (DBFW MRF): a multicomponent approach. Magn Reson Med 81(5):3032–3045. https://doi.org/10.1002/mrm.27628 (**Epub 2018 Dec 21. PMID: 30578569; PMCID: PMC6590362**)
99. Ostenson J, Damon BM, Welch EB (2019) MR fingerprinting with simultaneous T1, T2, and fat signal fraction estimation with integrated B0 correction reduces bias in water T1 and T2 estimates. Magn Reson Imaging 60:7–19. https://doi.org/10.1016/j.mri.2019.03.017 (**Epub 2019 Mar 23. PMID: 30910696; PMCID: PMC6581466.**)
100. Marty B, Carlier PG (2020) MR fingerprinting for water T1 and fat fraction quantification in fat infiltrated skeletal muscles. Magn Reson Med 83(2):621–634. https://doi.org/10.1002/mrm.27960 (**Epub 2019 Sep 10 PMID: 31502715**)

101. Jaubert O, Arrieta C, Cruz G, Bustin A, Schneider T, Georgiopoulos G, Masci PG, Sing-Long C, Botnar RM, Prieto C (2020) Multi-parametric liver tissue characterization using MR fingerprinting: simultaneous T1, T2, T2 *, and fat fraction mapping. Magn Reson Med 84(5):2625–2635. https://doi.org/10.1002/mrm.28311 (**Epub 2020 May 13 PMID: 32406125**)
102. Jiang Y, Hamilton JI, Lo W-C, Wright KL, Ma D, Coristine AJ, Seiberlich N, Gulani V, Griswold MA (2017) Simultaneous T1, T2 and diffusion quantification using multiple contrast prepared magnetic resonance fingerprinting. Proc Intl Soc Mag Res Med 1171
103. Zhang Y, Wells SA, Hernando D (2019) Stimulated echo based mapping (STEM) of T 1, T 2, and apparent diffusion coefficient: validation and protocol optimization. Magn Reson Med 81(1):167–181. https://doi.org/10.1002/mrm.27358